High-energy synchrotron x-ray techniques for studying irradiated materials

Jun-Sang Park
Advanced Photon Source, Argonne National Laboratory, Lemont, Illinois 60439, USA

Xuan Zhang
Nuclear Engineering Division, Argonne National Laboratory, Lemont, Illinois 60439, USA

Hemant Sharma and Peter Kenesei
Advanced Photon Source, Argonne National Laboratory, Lemont, Illinois 60439, USA

David Hoelzer
Materials Science and Technology Division, Oak Ridge National Laboratory, Oak Ridge, Tennessee 37831, USA

Meimei Li
Nuclear Engineering Division, Argonne National Laboratory, Lemont, Illinois 60439, USA

Jonathan Almer[a)]
Advanced Photon Source, Argonne National Laboratory, Lemont, Illinois 60439, USA

(Received 23 October 2014; accepted 23 January 2015)

High performance materials that can withstand radiation, heat, multiaxial stresses, and corrosive environment are necessary for the deployment of advanced nuclear energy systems. Nondestructive in situ experimental techniques utilizing high energy x-rays from synchrotron sources can be an attractive set of tools for engineers and scientists to investigate the structure–processing–property relationship systematically at smaller length scales and help build better material models. In this study, two unique and interconnected experimental techniques, namely, simultaneous small-angle/wide-angle x-ray scattering (SAXS/WAXS) and far-field high-energy diffraction microscopy (FF-HEDM) are presented. The changes in material state as Fe-based alloys are heated to high temperatures or subject to irradiation are examined using these techniques.

I. INTRODUCTION

The deployment of advanced nuclear energy systems depends critically on the development of advanced high performance materials that can tolerate extreme environments of intense radiation fields, high temperature, stress, and corrosion. Life extension of existing nuclear power plants relies on understanding irradiation-induced material degradation after long-term service. Designing radiation, heat, and corrosion-resistant materials and predicting the response of materials in extreme nuclear environments are two grand challenges for future growth of nuclear energy.

Irradiation generates a large population of point defects and their complexes in a crystalline solid. Further evolution of these defects leads to formation of extended defect structures, such as dislocation loops, stacking fault tetrahedra, voids, and helium bubbles. In certain cases, irradiation can also introduce second-phase precipitation and phase transformations in the parent (matrix) phase. The formation of a given type of defect structure is dependent on material chemistry, microstructure, irradiation temperature, dose, and dose rate. Uniformly distributed dislocation loops are typically formed at low doses and low temperatures ($T < 0.3T_m$, where T_m is the melting point).[1] Heterogeneous dislocation loop structures and dislocation networks are observed at intermediate and high doses.[2] Significant void and helium bubble formation occurs at higher irradiation temperatures ($0.3T_m < T < 0.5T_m$).[3] Phase transformations have been observed in various alloys under irradiation due to ballistic transport and radiation-enhanced diffusion.[4]

Each of these microstructural changes can affect the physical and mechanical properties of a material and severely degrade the reliability and lifetime of nuclear reactor components. Common degradation phenomena in nuclear reactor materials include low-temperature embrittlement, void swelling, irradiation creep, high-temperature grain boundary helium embrittlement, and irradiation-induced stress corrosion cracking.[5] Characterization and quantification (number density, mean size, size distribution, etc.) of these irradiation-induced defects and understanding their effects on macroscopic mechanical properties are of fundamental importance for addressing the two grand challenges.

Contributing Editor: Djamel Kaoumi
[a)]Address all correspondence to this author.
e-mail: almer@aps.anl.gov
DOI: 10.1557/jmr.2015.50

https://doi.org/10.1557/jmr.2015.50 Published online by Cambridge University Press

The macroscopic mechanical response of a material is a result of many competing dynamic processes originating from atomic and microscopic length scales. At the current stage, however, the relationship between these dynamic processes and resulting macroscopic mechanical response has relied largely on phenomenological or empirical models. These models are not particularly effective in providing a good description of material behavior beyond the testing conditions and do not truly capture the fundamental physics of these dynamic processes. To describe the macroscopic material behavior under any external conditions (such as temperature and strain rates), multiscale modeling that captures the fundamental physics at the smaller length scales combined with appropriate linking assumptions is necessary. Furthermore, such modeling efforts must be closely coupled with in situ experiments at appropriate length scales.

Third-generation synchrotron sources produce high-brilliance, hard x-rays, which allow nondestructive in situ measurements with high spatial and temporal resolution. For example, the internal stresses in a polycrystalline material were determined to elucidate the behaviors of constituent phases in the material during tensile, compressive, and/or cyclic loading.[6] Strain and texture mapping around a crack tip by in situ synchrotron x-ray diffraction provided a better understanding of deformation and crack propagation mechanisms under static and fatigue loading.[7] Combined imaging studies, such as grain structure mapping by diffraction contrast tomography and crack mapping by synchrotron x-ray microtomography in corrosive environments, have provided insight into the dynamic interaction of a growing crack with crystal structure and the contribution of different boundary types to cracking resistance.[8] These studies point to critical and available tools which can be used to understand the micromechanical behavior of materials relevant to nuclear energy. Information obtained from these experimental techniques is crucial for multiscale modeling efforts.

In this study, we demonstrate the application of two high energy x-ray techniques to study nuclear-relevant materials. The first is simultaneous small-angle and wide-angle x-ray scattering (SAXS/WAXS) with in situ thermo-mechanical loading. Here, the grain ensemble average information on a polycrystalline material is obtained, over a wide range of size scales ranging from 0.1 to 100 nm. The second is far-field high-energy diffraction microscopy (FF-HEDM) where information about individual grains in a polycrystalline material is obtained.[9] FF-HEDM is distinguished from a related technique of near-field HEDM, in that the former provides high resolution information on lattice parameters, orientations, and center-of-mass positions within grains, while the latter provides detailed information on grain shapes.[10] Data from these techniques can provide critical tests to existing micromechanical models, enable more accurate predictions of mechanical performance of nuclear reactor materials subjected to extreme environments and, in doing so, facilitate the development of new reactor materials.

II. METHODS

A. Oxide dispersion-strengthened (ODS) steels measured with SAXS/WAXS

The 14YWT samples investigated are nanostructured ferritic alloys. They contain ultrafine grains and high densities of nanometer-sized oxide particles. These nanometer-sized oxide particles are also referred to as Y-, Ti-, and O-enriched nanoclusters and provide excellent high-temperature strength and creep properties, good low-temperature fracture toughness, and high resistance to neutron irradiation. Two heats of 14YWT were examined, namely, 14YWT-CR4 and 14YWT-SM12. Their chemical compositions are listed in Table I. The 14YWT-CR4 heat was made from argon gas atomized prealloyed powders made by Crucible Research. It was extruded at 850 °C, heat-treated at 1000 °C for 1 h, and rolled parallel to the extrusion direction at 600 °C to 40% reduction in thickness (RIT). The 14YWT-SM12 heat was produced by a mechanical alloying process using gas-atomized powder produced by Special Metals Inc. It was extruded at 850 °C, annealed at 1000 °C for 1 h followed by rolling parallel to the extrusion direction at 1000 °C to 50% RIT. Due to improved mechanical alloying conditions, SM12 has significantly lower C, N, and O levels than CR4. For both heats, miniature sheet-type tensile samples were machined, with the rolling direction parallel to the loading axis. The nominal yield strength of heat SM12 is approximately 1100 MPa at room temperature and decreases continuously with increased temperature; at 800 °C, its yield strength is 250 MPa.[11] The nominal dimensions of the gauge section of these samples were 5 mm × 1.2 mm × 0.75 mm.

Simultaneous SAXS/WAXS measurements were conducted on the 14YWT samples using the setup shown in Fig. 1 at the 1-ID beamline of the Advanced Photon Source (APS). Four GE-RT41 panels recorded the WAXS signals at a sample–detector distance (Z_{WAXS}) of 2103 mm and were arranged to form a hole in the center through which the transmitted direct beam and the SAXS signals could pass. The transmitted direct

TABLE I. The chemical compositions of the two heats of 14YWT examined in this work.

wt%	Fe	Cr	W	Ti	Y	O	N	C
14YWT-CR4	Bal.	13.46	1.03	0.24	0.23	0.21	0.02	0.05
14YWT-SM12	Bal.	14.33	2.16	0.26	0.20	0.10	0.01	0.02

https://doi.org/10.1557/jmr.2015.50 Published online by Cambridge University Press

beam and SAXS signals were recorded downstream using an ion chamber and Scint-X DXI-11000 camera (Scint-X, Kista, Sweden) (Z_{SAXS} = 3800 mm), respectively. Each GE detector had 2048 × 2048 pixels^2 and a 0.2 mm pixel pitch, while the ScintX detector consisted of 2012 × 1340 pixels^2 and a 0.018 mm pixel pitch (2x binned mode). The x-ray energy was 70 keV and vertically focused at the SAXS detector position using refractive lenses[12] located approximately 20 m upstream of the SAXS detector, with an effective beam size at the sample of 0.1 × 0.05 mm^2 ($H \times V$). A NIST standard CeO_2 powder[13] was measured prior to sample measurements to refine the WAXS instrument parameters including sample–detector distances, beam position, and detector distortions. As discussed for the FF-HEDM data below, calibrations were accurate to $\Delta d/d < 10^{-4}$ for all CeO_2 rings recorded. SAXS data were similarly calibrated using a glassy carbon standard.[14] Typical WAXS and SAXS images for the ODS steel are shown in the figure, along with the definition of detector azimuth angle, η (X_L is along η = 0°), and radial distance, ρ. The SAXS detector was offset from the direct beam to maximize the Q-space coverage.

In addition to ex situ measurements, the SM12 samples were also subjected to in situ thermo-mechanical deformation, using a MTS servo-hydraulic machine and a clamshell design IR furnace, as described by Wang et al.[15] The sample was first heated from room-temperature to 800 °C, at 0.9 °C/s, while under load control (85 MPa) to account for thermal expansion of the sample and grips. The sample was then deformed in displacement control at 5 × 10^{-5} mm/s until nonuniform deformation along the gauge section (necking) was observed. During the entire process, both SAXS and WAXS signals were recorded at 10 s intervals.

B. High-temperature ultrafine-precipitate-strengthened (HT-UPS) steels measured with FF-HEDM

HT-UPS austenitic stainless steels are candidates for structural and cladding applications in the next-generation advanced nuclear reactors because of improved creep resistance and irradiation tolerance over traditional 316 stainless steel.[16] The nominal composition of the HT-UPS stainless steel samples examined in this work is shown in Table II.

The samples were solution annealed at 1200 °C for 1 h. A set of transmission electron microscopy (TEM) disk samples (3 mm diameter × 0.2 mm thick) were extracted from a single batch of HT-UPS steel. A subset of these was neutron-irradiated to 3 dpa at 500 °C at the Advanced Test Reactor at the Idaho National Laboratory. When measured at the APS, the activity of a sample was less than or equal to 50 μSv/h at a distance of 30 cm. Both neutron-irradiated samples and nonirradiated control samples were individually mounted in a double-contained Kapton sample holder [Fig. 2(a)] and sealed at the Irradiated Materials Laboratory at Argonne National Laboratory (ANL). The double-contained samples were then transferred to the APS 1-ID beamline for ex situ FF-HEDM experiments where several layers of the irradiated and control samples were interrogated with high energy x-rays by translating the sample with respect to the x-ray beam [Fig. 2(b)].

TABLE II. The chemical compositions of the HT-UPS stainless steel examined in this work.

wt%	Fe	Cr	Ni	Mo	Mn	Si	P	Ti	Nb	V	C	N
HT-UPS	Bal.	13.90	16.00	2.59	2.00	0.11	0.04	0.28	0.11	0.53	0.06	0.02

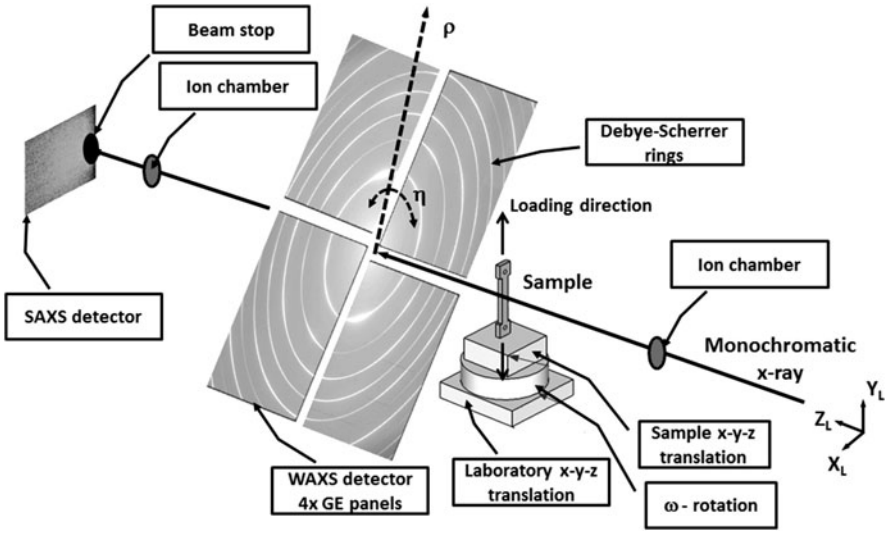


FIG. 1. Schematic of SAXS/WAXS measurements, including actual images from an ODS sample and definitions of laboratory coordinates X_L–Y_L–Z_L and detector coordinates η and ρ.

https://doi.org/10.1557/jmr.2015.50 Published online by Cambridge University Press

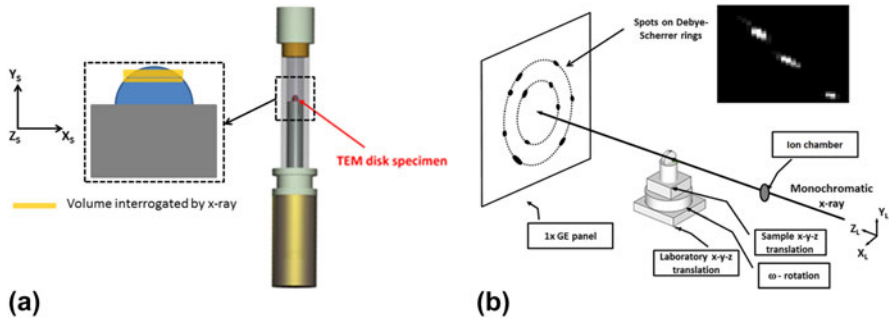


FIG. 2. (a) Schematic of the irradiated HT-UPS sample measured, with the disk-shaped sample sitting on a sample holder and encapsulated in two layers of Kapton tube. An enlarged view of the sample illustrates the volumes interrogated by the x-rays. (b) Schematic showing full FF-HEDM setup, along with actual diffraction spots.

FF-HEDM measurements were conducted as illustrated in Fig. 2(b), with a x-ray beam energy of 65.351 keV and beam size of 2×0.2 mm^2 ($H \times V$). A single panel GE-RT41 detector was placed approximately 909 mm downstream of the sample and nominally centered on the incident beam. As opposed to the smoothly varying intensities associated with the fine-grained ODS steel samples (Fig. 1), the coarser-grained HT-UPS samples produced spotty diffraction patterns which ensured that individual grains could be measured using the FF-HEDM technique. Datasets were obtained by taking a series of GE detector images at 0.5° intervals in ω over a range of −180° to +180°, where ω is the rotation about Y_L and defined such that at ω = 0° the sample S and laboratory L coordinate systems are identical. Three sample layers were measured by translating the sample along Y_L a distance of 0.2 mm/layer. NIST CeO_2 powder patterns were measured at ω = 180° and −180° to determine the instrument parameters. The residuals between the fitted and expected *d*-spacings, as expressed as pseudo-strains, were on the order of 1×10^{-5} establishing the instrumental uncertainty (Fig. 3). Furthermore, diffraction spots from a single crystal standard such as the ruby standard from NIST[17] are used to determine the angular orientation of the detector with respect to the direct beam.

To obtain grain-resolved information from the FF-HEDM data, the diffraction spots for the {111} and {200} crystallographic planes emanating from individual grains in the illuminated volume were identified using intensity thresholding. Their positions (or the associated scattering vectors) were corrected for systematic distortions using the instrument parameters obtained from CeO_2 data. These spots were then indexed[18,19] to obtain the center of masses (COMs), crystallographic orientations, and elastic strains of the constituent grains in the illuminated volume.

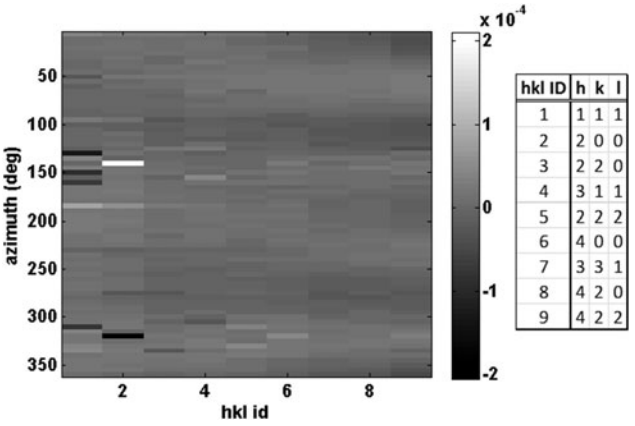


FIG. 3. Instrument parameter optimization results for the CeO_2 powder for single-panel GE used for FF-HEDM, showing pseudo-strains for different families of crystallographic planes and η (binned in 5° segments). Color bar denotes the pseudo-strains. The mean value is 1×10^{-5} with standard deviation on the same order.

III. RESULTS

A. SAXS/WAXS measurements on ODS steels

Figure 4 shows a portion of the η-integrated WAXS diffraction pattern for the as-received SM12 and CR4 samples, magnified to emphasize the minor phases. The higher content of C and O in CR4 leads to extensive precipitation of primarily the $M_{23}C_6$ phases. Here, we employ a general notation, $M_{23}C_6$ for carbides with crystal lattice of $Cr_{23}C_6$ where Cr is often replaced with Ni, Mo, Fe, and W. Traces of TiN and $Y_2Ti_2O_7$ are also present. In contrast, the SM12 diffraction pattern is much cleaner, with Ti(C,N) as the only identifiable precipitate phase with a lattice parameter of 4.298 Å. Since the lattice parameter is 4.327 Å for TiC and 4.242 Å for TiN, the precipitate composition is calculated to be $TiC_{0.66}N_{0.34}$ assuming Vegard's law. There are no visible diffraction peaks from Yi–Ti–O phases in SM12, which is attributed to the small volume fraction and small sizes of the oxide particles (4–5 nm on average observed in TEM) which leads to substantial peak broadening.

Figure 5(a) shows the azimuthally averaged SAXS intensity profiles for the SM12 and CR4 samples. The small volume fraction and sizes of the Y–Ti–O particles make them unresolvable by WAXS. SAXS provides an opportunity to make up the missing information. As seen in Fig. 5(a), there are significant differences between the

https://doi.org/10.1557/jmr.2015.50 Published online by Cambridge University Press

alloys: at high Q values, the intensity extends to higher Q for SM12 than for CR4, which indicates that the smallest features in SM12 are smaller than those in CR4; at lower Q values, CR4 shows a transition from the Porod regime to the Guinier regime while SM12 does not (due to the Q-min limitation of the experimental setup), which indicates that there are features of tens of nanometers in size in CR4 while not in SM12. The volume distributions of the scattering domains, obtained from those Q-plots by using the software Irena,[20] are shown in Fig. 5(b). The majority of the particles in SM12 have an average size of 4–5 nm, which is smaller than those in CR4 which have an average of 6–7 nm. As seen in Figs. 5(c) and 5(d) for the SM12 and CR4 samples respectively, the energy filtered TEM Fe M-jump ratio observations reveal that these particles are Y–Ti–O. In CR4, there is a significant group of particles with sizes of tens of nanometers. These large particles contribute to the diffraction signal observed in Fig. 4.

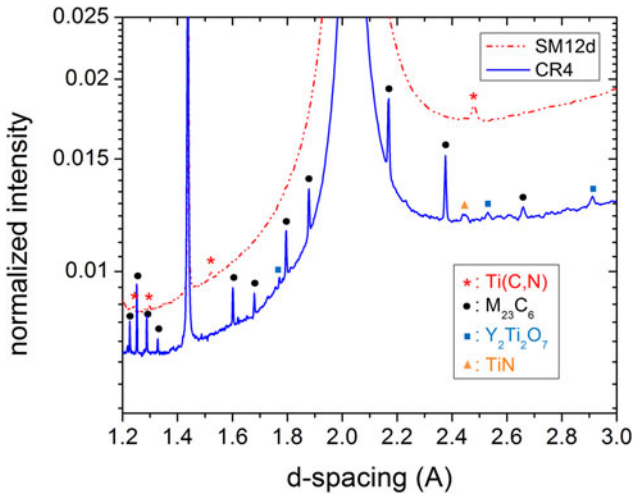


FIG. 4. WAXS diffraction pattern (over partial d-spacing range) of the as-received SM12 and CR4 samples with precipitate peaks labeled. The intensity is normalized to a value of 1 for the strongest reflection in both samples, Fe {110}, which is located at d = 2.03 Å.

The phase-specific response of the SM12 sample to applied deformation at 800 °C was quantified by fitting pseudo-Voigt functions to diffraction peaks from each phase, and the results are shown in Fig. 6. Lattice strains were computed from diffraction peak shifts, using $\varepsilon_{nn} = \frac{d_0^n - d^n}{d_0^n}$, where ε_{nn} is the lattice strain measured along measurement direction, $\boldsymbol{n}$, d_0^n is the reference d-spacing measured along $\boldsymbol{n}$ in the unloaded condition at a given temperature and d^n is the d-spacing measured along $\boldsymbol{n}$ at load at the same temperature. The lattice

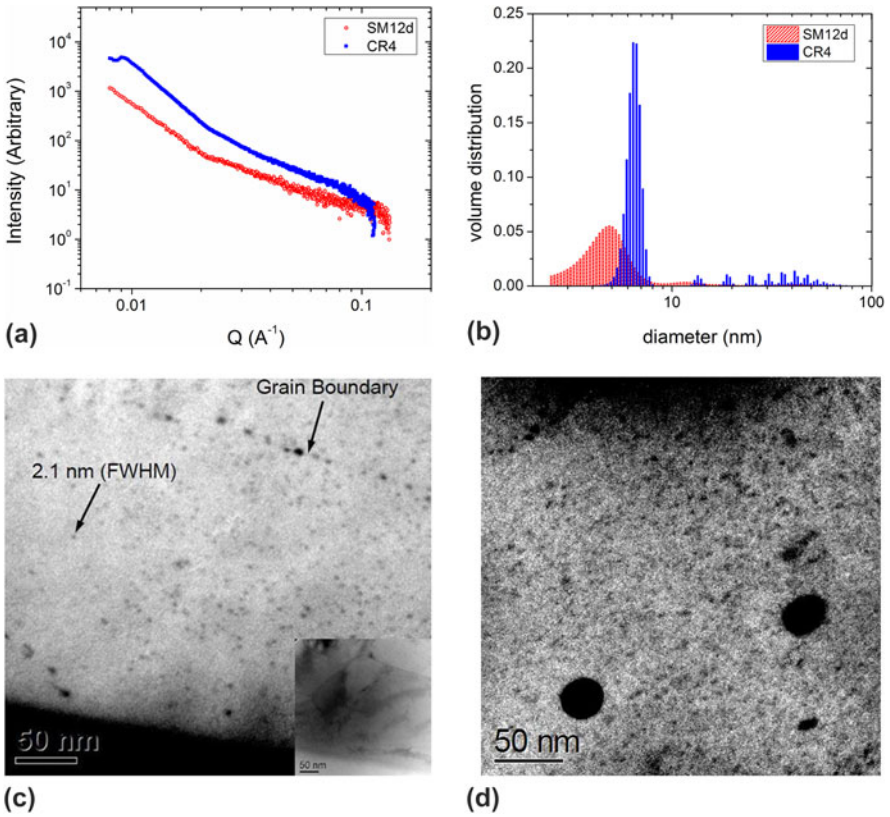


FIG. 5. Results for ODS as-received samples. (a) Azimuthally integrated SAXS intensity versus Q for the as-received SM12 and CR4 samples. (b) Derived particle volume distributions from the SAXS data in (a). (c) EFTEM image of as-received SM12 showing the oxide particles, and (d) EFTEM image of as-received CR4 showing the precipitate particles.

https://doi.org/10.1557/jmr.2015.50 Published online by Cambridge University Press

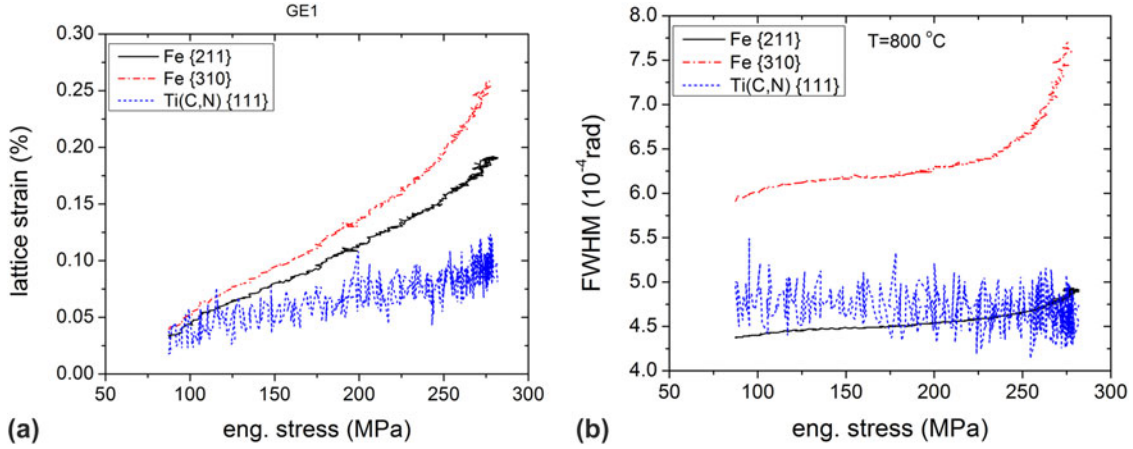


FIG. 6. Phase-specific response of SM12 specimen to applied stress at 800 °C: (a) lattice strain of Fe {211}, {310}, and Ti(C,N) {111} along the loading direction. (b) FWHM of the same reflections.

strains are presented as a function of applied stress in Fig. 6(a) for the Fe matrix grains, whose {211} planes or {310} planes are parallel to the loading axis, and the Ti(C, N) precipitate grains, whose {111} planes are parallel to the loading axis. The lower intensity of the precipitate peaks leads to higher scatter in the data, but trends between phases can still be delineated. In particular, while the slope of the Ti(C, N) {111} strain is small but constant versus applied stress, those from the Fe {211} and {310} reflections change slope at a value of about 230 MPa. Figure 6(b) shows the corresponding full width at half maximum (FWHM) values. The Fe matrix peaks, particularly the {310}, broaden significantly above 230 MPa while the precipitate peak is essentially constant.

B. HEDM measurements on HT-UPS

Before presenting individual grain data, the "powder average" scattering patterns of HT-UPS samples are shown in Fig. 7. These patterns were computed for both control and irradiated samples, by summing images from all ω orientations (−180° – +180°). Noteworthy is the absence of secondary phases in either the initial or irradiated specimens, indicating phase-stability under the irradiation and both a broadening and slight shift to higher 2θ values (corresponding to smaller *d*-spacings) after irradiation for the austenite Fe-peaks.

Diffraction spots from {111} and {200} planes were used in the FF-HEDM analysis as their intensities were well above the background levels of the area detector. Through the FF-HEDM analysis, 979 grains were indexed in the control sample for all three layers, and 1075 grains in the irradiated sample for all three layers with a completeness of 0.7 or higher. The completeness of a grain is defined as the number of measured diffraction spots divided by the number of expected diffraction spots. For a particular grain in the aggregate, 28 diffractions spots were anticipated and at least 19

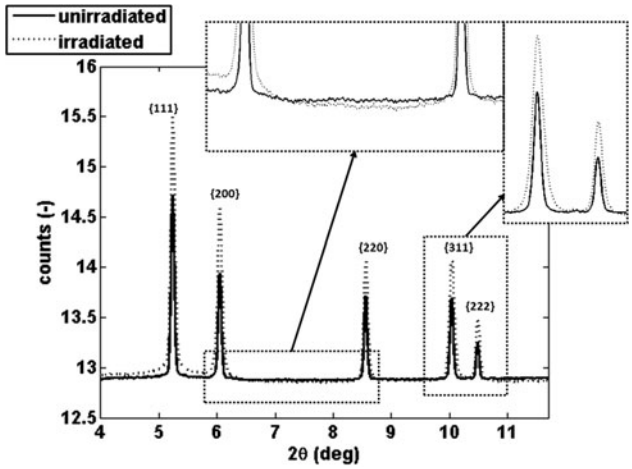


FIG. 7. Integrated "powder" lineouts for the HT-UPS samples in irradiated and control states. Counts are in a logarithmic scale. The peak widths in the irradiated sample are larger than those in the control sample, and shifted to slightly larger values of 2θ. Note the absence of secondary phases in both samples.

diffraction spots were required. The volume of a grain is estimated by enforcing that the diffraction spots that belong to a grain have matching intensities and normalizing the diffraction spot intensities with the incident flux.[21] Figures 8 and 9 show the COMs and crystallographic orientations of the grains found in one of the three layers in the control and irradiated samples, respectively. Rodrigues parameterization is used to represent the crystallographic orientation of the grains with respect to the sample.[22] While there are a few outliers, the majority of grain COMs are within the sample dimensions. These outliers were removed for subsequent analyses. It is also worthwhile to note that the completeness is, in general, lower for the irradiated sample. This may be attributed to the fact that the diffraction spots from the irradiated sample are smeared significantly

https://doi.org/10.1557/jmr.2015.50 Published online by Cambridge University Press

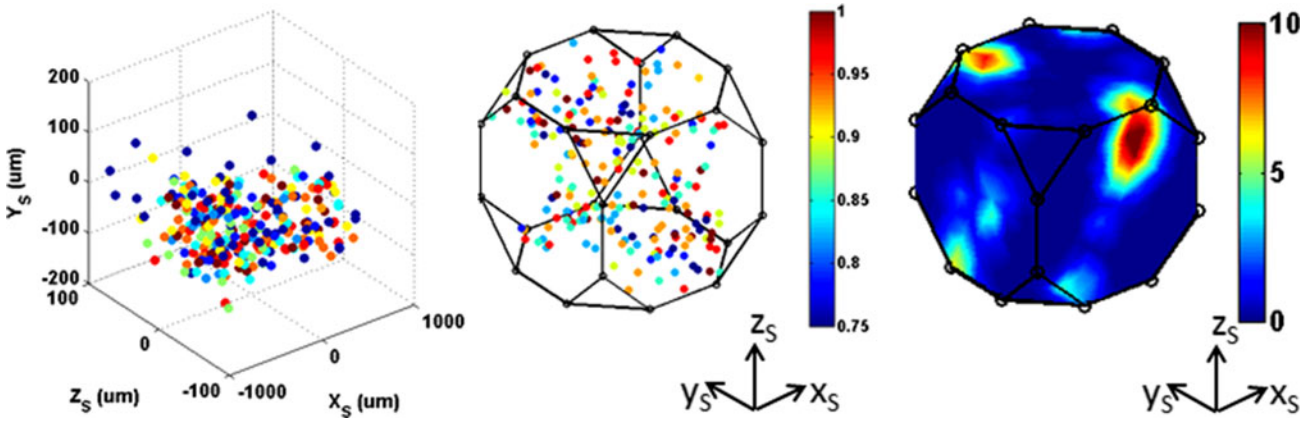


FIG. 8. Grain COMs (left) and crystallographic orientations (center) obtained from HEDM measurements of a layer of the control sample. Colors denote completeness. ODF computed from the crystallographic orientations of the constituent grains in the layer (right). Color denotes MUDs.

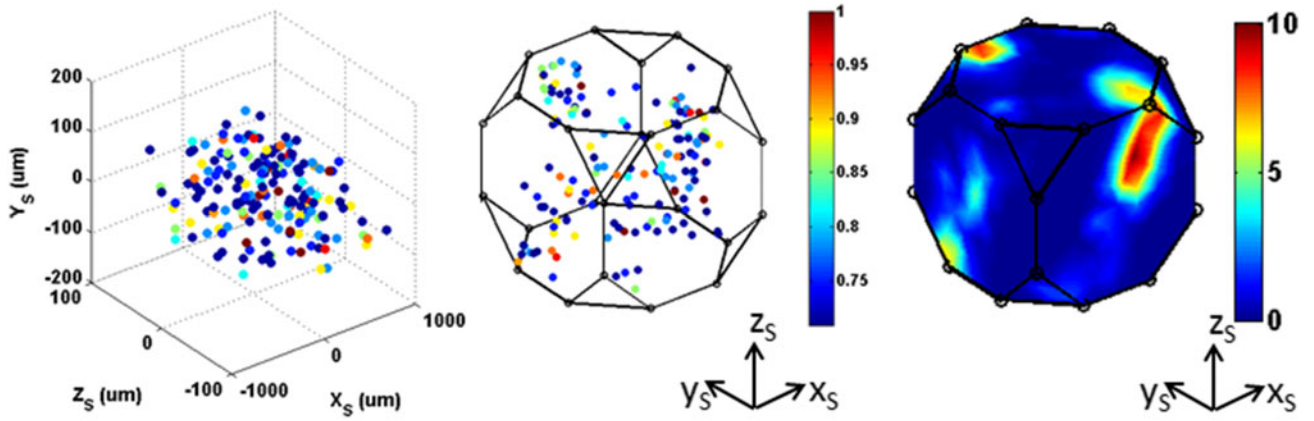


FIG. 9. Grain COMs (left) and crystallographic orientations (center) obtained from HEDM measurements of a layer of the irradiated sample. Colors denote completeness. ODF computed from the crystallographic orientations of the constituent grains in the layer (right). Color denotes MUDs.

compared to those obtained from control sample, which is further discussed below. Also plotted in the figures are the orientation distribution functions (ODFs) for the two states computed from the crystallographic orientations of individual grains. The initial crystallographic texture is significant, with a maximum multiple of uniform distribution (MUD) of about 10 and attributed to directional thermo-mechanical deformation (rolling) during material processing. As anticipated, this initial crystallographic texture does not evolve with irradiation.

The smearing of diffraction spots from individual grains after irradiation has been observed by x-ray Laue microdiffraction techniques[23,24] which are similar, but distinct from HEDM. In these studies, changes in the state of the materials due to irradiation were observed in the limited number of grains that these techniques can interrogate. In the present case, to quantitatively determine differences between the irradiated and control samples, results from two-dimensional Gaussian fits to individual diffraction spots were compiled for the two specimens for a statistically significant number of grains. Figures 10 and 11 show the histograms of the FWHM values in the radial (ρ) and azimuthal (η) directions. These figures show that the FWHM values from an irradiated sample are broader on average, and have a broader distribution, than those from the control sample, in both directions measured. This indicates that irradiation may have introduced significant modifications at the grain and subgrain scale. The accumulation of irradiation induced defects such as point defect, clusters, voids, and dislocation loops can contribute to such peak broadening or peak splitting.[25–28] Furthermore, irradiation-induced recrystallization[29,30] can also lead to the formation of subgrains, which would also increase the FWHM of the diffraction spots consistent with these observations.

IV. DISCUSSION

FF-HEDM and SAXS/WAXS are two distinct, but related, x-ray techniques which can reveal key aspects of

https://doi.org/10.1557/jmr.2015.50 Published online by Cambridge University Press

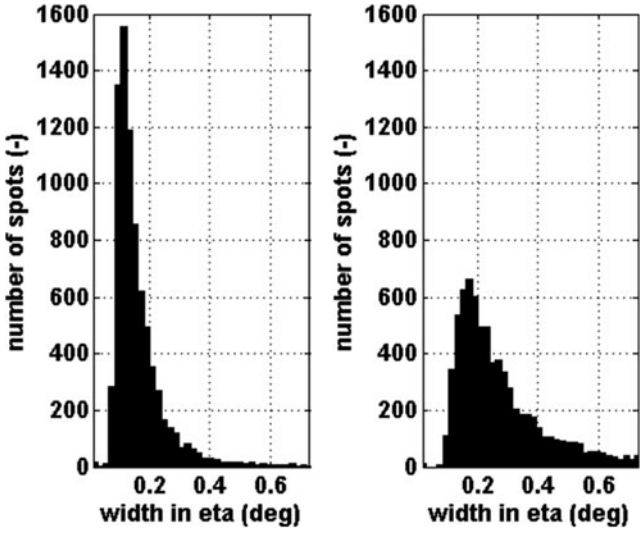


FIG. 10. The FWHM of the diffraction spots from Fe {111} and {200}, along η for the nonirradiated (left) and irradiated (right) samples.

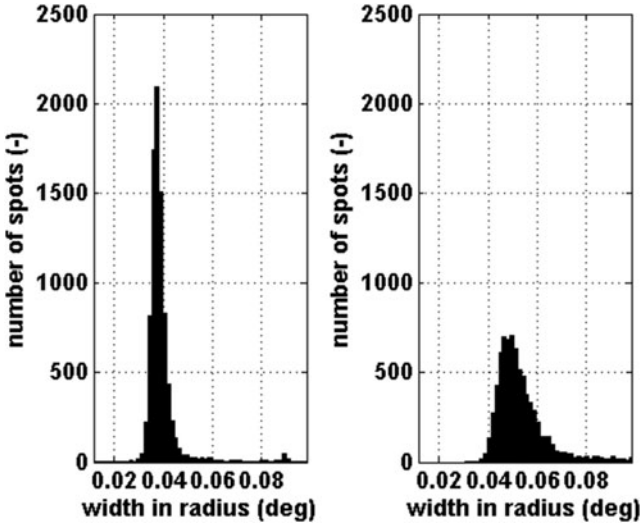


FIG. 11. The FWHM of the diffraction spots from Fe {111} and {200}, along ρ for the nonirradiated (left) and irradiated (right) samples.

nuclear-relevant materials. Both use high-energy x-rays to penetrate samples that are 1 mm or thicker and generate forward scattering which can be efficiently collected with area detectors. This provides a rich set of microstructural information on crystalline materials, even for low volume fraction phases.

In the case of the fine-grained materials like the ODS steels presented, grain-averaged ("powder") SAXS/WAXS can be used to evaluate even nanophased materials, including their response to applied stress and temperature. When above a sufficient size such that size-induced broadening is not too dominant, WAXS information can be obtained even for minor phases, to evaluate intraphase composition (as in the case of Ti(C,N)) and strains. The ability to distinguish a nanophase using WAXS is a function of both its volume fraction and size-induced broadening. Here, we estimate the broadening by considering only the domain size effect (neglecting microstrain contributions): for 70 keV x-rays ($\lambda = 0.0177$ nm), the broadening α (in radians) for a feature size b (in nm) can be estimated by:

$$\alpha = \frac{0.9\lambda}{b\cos\theta} \quad , \tag{1}$$

where the cos θ is approximately 1 for the experimental geometry used in this work.[31] Instrumental broadening is assumed to be negligible. Using this equation, α is 1.6×10^{-3} radians for a feature size of 10 nm (an upper limit for the nanophased oxides given by the SAXS results). The FWHM values for Fe {211}, Fe {310}, and Ti(C,N) {111} peaks measured at room temperature are 4.1×10^{-4} radians, 5.1×10^{-4} radians, and 5.2×10^{-4} radians, respectively. These values are over four times larger than that anticipated for the nanophases with a 10 nm feature size. Furthermore, the volume fraction for the nanophase oxides is on the order of only 1% (0.3 wt% total Y_2O_3 added for alloying) and can be in amorphous state.[32] These effects push the features like nanophases below the WAXS sensitivity limit of even high-flux synchrotron sources.

For smaller particles and clusters, SAXS provides the ability to capture features on the nanometer level. It should be noted that any inhomogeneous feature on this size-scale may be studied, with the sensitivity proportional to the feature volume and square of the electron-density contrast between the feature and average sample density. For this reason, voids and bubbles provide a particularly high contrast and may be studied at lower concentrations than equivalent amounts of (higher density) precipitate phases.[33,34]

The in situ loading results of SM12 from WAXS in Fig. 6 show the complex nature of the micromechanical stress state and its evolution with applied load. Figure 6(a) shows that the lattice strain measured along the loading direction for {211} and {310} in the Fe matrix shows an inflection at an applied stress of 230 MPa while the strain {111} in the Ti(C,N) phase does not. In fact, the {111} in the Ti(C,N) continues to increase steadily up until ~280 MPa where the experiment was terminated. Meanwhile, in Fig. 6(b), the FWHM values of Fe {211} and Fe {310} again show a large inflection near 230 MPa while Ti(C,N) {111} remains constant. These inflection points in lattice strains and FWHM indicate that the Fe matrix has yielded. While the relative strength to stiffness ratios can lead to the stronger and stiffer phase to yield first in a multiphase material,[35] it is more likely that the state of stress in the Fe-matrix is reorienting to a yield vertex such that polyslip can occur.[36–38]

https://doi.org/10.1557/jmr.2015.50 Published online by Cambridge University Press

The distinction between WAXS and HEDM methods lies in the ability to separate the individual spots on the diffraction patterns. This will in turn depend on the state of the material and the number of grains in the volume illuminated by x-ray crystallography of the material, fidelity of the instrument, and analysis software. For cubic materials as measured in this work, and the experimental approach utilized, HEDM can be used for up to approximately 10,000 grains, although changes in the state of the material induced by irradiation or applied plastic deformation can reduce this number significantly. It is also worthwhile to note that the WAXS setup used for the SAXS/WAXS measurements can be used for the FF-HEDM measurements, possibly pushing the upper limit even higher.

Unlike the "powder" WAXS method where grain-averaged data are collected, the FF-HEDM method preserves the spatial information and neighborhoods of the individual grains in an aggregate. This opens new opportunities for studying materials relevant to nuclear applications; the effect of irradiation can be investigated on a grain-by-grain basis and individual diffraction spots that belong to a particular grain. To illustrate this point, we examine lattice constants in more detail. Comparing the two states of HT-UPS, the powder pattern averages (Fig. 7) in the control and irradiated states are 3.597 Å and 3.595 Å, respectively, indicating a small but measurable change in the average microstructure. Using HEDM data, the lattice constants of the indexed grains can be plotted against the relative grain radii (Fig. 12) to reveal the distribution of lattice constants.

For the control sample, the distribution is relatively constant with radius, with some smaller grains showing some decrease. One possibility for this decrease is the presence of significant grain-boundary solute segregation, which has been observed in such alloys. Such segregation could shift average peak positions (due to intragrain compositional changes) preferentially in the smallest grains with highest grain boundary/bulk fractions. The distribution in lattice parameters in the irradiated sample is considerably broader and with a volume-weighted reduction in lattice parameter of $\sim 4.7 \times 10^{-4}$ Å. This reduction is consistent with the powder-average results, providing a check on the overall statistics. While a full explanation of this result requires a detailed knowledge of the defect structures, which cannot be obtained by the x-ray techniques alone, some general points can be made. The reduction suggests that there is a substantial amount of vacancy types of defects present, and/or the average chemistry in the matrix has changed to decrease the lattice parameter, since a net accumulation of interstitial types of defects will expand the lattice.[30,39–41] The variation among the grains suggests that the size, dislocation structure, and orientations of the grains could all matter for defect accumulation/recovery as well as for solute segregation in alloy systems under irradiation.[42–45] Further investigations, including measured grain orientations and direction-dependent broadening, are planned to investigate these possibilities more fully.

V. OUTLOOK

The data presented here illustrate how high-energy x-rays can be used to nondestructively study the nuclear energy-relevant materials on a wide-range of length scales; from mm down to μm in real-space and down to the atomic level in reciprocal space. The microstructural effects of irradiation can be studied in great detail. In particular, the grain-scale HEDM data provide an opportunity to reveal irradiation-induced defects in new ways. Unlike the WAXS method, the HEDM data are no longer subject to crystallographic fiber averages; spatial information about individual grains and their neighborhoods are preserved. For example, Figs. 10 and 11 illustrate that unlike the conventional line profile analysis commonly applied to WAXS data,[46–48] we can study the evolution of individual spots that belong to a particular grain to investigate the relationship between irradiation-induced

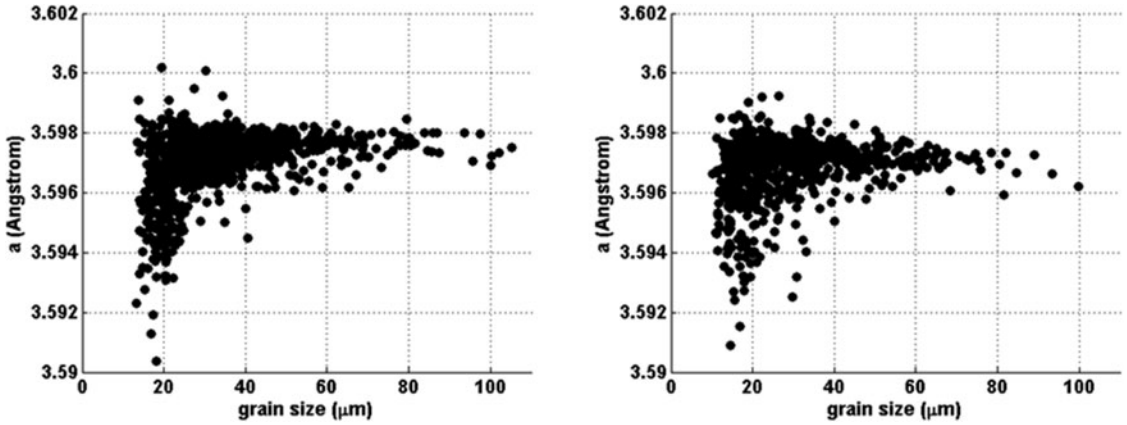


FIG. 12. Lattice constant versus grain radii for control (left) and irradiated (right).

https://doi.org/10.1557/jmr.2015.50 Published online by Cambridge University Press

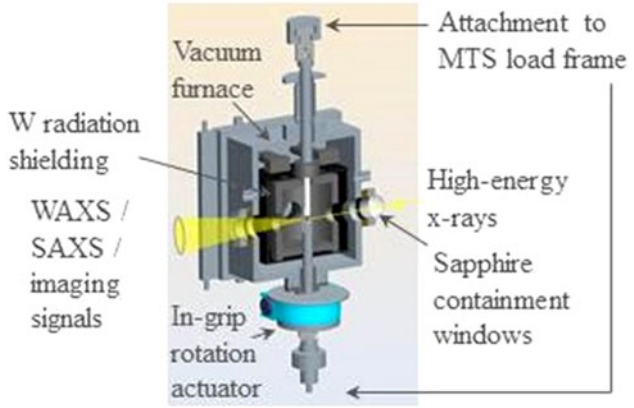


FIG. 13. Schematic of an in situ thermo-mechanical environment for studying irradiated materials with high-energy x-ray techniques.

damage in the grain and its crystallographic orientation or neighborhood. A promising approach would be developing forward-modeling approaches, in which a "virtual" sample is instantiated with a defined population of defects and defect types. Diffraction spots are then projected to the detector and compared with the measured results.[49,50] This would in turn allow material models at such length scales to be examined and calibrated[51,52] so that prediction of bulk properties does not have to rely only on empirical correlations.[53,54] Such a virtual sample can then be subjected to irradiation and/or thermo-mechanical loads, to further compare against experimental data as presented here.

Finally, we note that the ability to apply these x-ray techniques in concert with in situ environments on irradiated samples is crucial if such an approach is to be undertaken. One example of such an approach is a thermo-mechanical setup shown in Fig. 13, developed at ANL. This device will allow for simultaneous loading up to 2.5 kN and temperatures to 1200 °C on irradiated samples, with an internal rotation mechanism to permit FF-HEDM and tomography experiments. After commissioning in 2015, it is anticipated that other users may use this device for their own experiments.

ACKNOWLEDGMENTS

The research was sponsored by the U.S. Department of Energy, Office of Nuclear Energy, for the Nuclear Energy Enabling Technology (NEET) Program under Contract No. DE-AC02-06CH11357. This research used resources of the Advanced Photon Source, a U.S. Department of Energy (DOE) Office of Science User Facility operated for the DOE Office of Science by Argonne National Laboratory under Contract No. DE-AC02-06CH11357. Neutron-irradiated specimens were provided by the ATR National Scientific User Facility (NSUF) at the Idaho National Laboratory (INL). The authors would like to thank Collin Knight, Brandon Miller, and James Cole at the ATR NSUF, INL. The authors also would like to thank Loren A. Knoblich, Jakub P. Dobrzynski, Yiren Chen at the Irradiated Materials Laboratory, Brent A. Finney at Special Materials, John Vacca at Health Physics, Environment, Safety, and Quality Assurance, APS Radioactive Sample Safety Review Committee at ANL. Erika Benda and Ali Mashayekhi at the APS, ANL are thanked for designing and fabricating the specimen holders for the irradiated TEM specimen.

REFERENCES

1. S.J. Zinkle and B.N. Singh: Microstructure of neutron-irradiated iron before and after tensile deformation. *J. Nucl. Mater.* **351**(1–3), 269 (2006).
2. B.N. Singh and J.H. Evans: Significant differences in defect accumulation behavior between FCC and BCC crystals under cascade damage conditions. *J. Nucl. Mater.* **226**(3), 277 (1995).
3. H. Trinkaus, B.N. Singh, and A.J.E. Foreman: Glide of interstitial loops produced under cascade damage conditions: Possible effects on void formation. *J. Nucl. Mater.* **199**(1), 1 (1992).
4. H. Wollenberger: Phase-transformations under irradiation. *J. Nucl. Mater.* **216**, 63 (1994).
5. S.J. Zinkle and J.T. Busby: Structural materials for fission & fusion energy. *Mater. Today* **12**(11), 12 (2009).
6. D.R. Haeffner, J.D. Almer, and U. Lienert: The use of high energy X-rays for the advanced photon source to study stresses in materials. *Mater. Sci. Eng., A* **399**(1), 120–127 (2005).
7. M.R. Daymond, M.L. Young, J.D. Almer, and D.C. Dunand: Strain and texture evolution during mechanical loading of a crack tip in martensitic shape-memory NiTi. *Acta Mater.* **55**(11), 3929 (2007).
8. A. King, G. Johnson, D. Engelberg, W. Ludwig, and J. Marrow: Observations of intergranular stress corrosion cracking in a grain-mapped polycrystal. *Science* **321**(5887), 382 (2008).
9. H.F. Poulsen: Three-Dimensional X-Ray Diffraction Microscopy: Mapping Polycrystals and their Dynamics. *Springer Tracts in Modern Physics* Vol. 205; Springer-Verlag: Germany.
10. R. Suter, D. Hennessy, C. Xiao, and U. Lienert: Forward modelling method for microstructure reconstruction using x-ray diffraction microscopy: Single-crystal verification. *Rev. Sci. Instrum.* **77**, 123905, 2006.
11. D.T. Hoelzer, K.A. Unocic, E.T. Manneschmidt, and M.A. Sokolov: Reference Characterization of the Advanced ODS 14YWT-SM12 Heat Used in HFIR JP30/31 Neutron Irradiation Experiment, *Fusion Reactor Materials Program DOE/ER-0313-0352*, Vol. 52, 2012.
12. S.D. Shastri, J. Almer, C. Ribbing, and B. Cederstrom: High-energy X-ray optics with silicon saw-tooth refractive lenses. *J. Synchrotron Radiat.* **14**, 204 (2007).
13. National Institute of Standards and Technology: *X-Ray Powder Diffraction Intensity Set (Quantitative Powder Diffraction Standard)*, USA, 2012. https://www-s.nist.gov/srmors/view_detail.cfm?srm=674B.
14. F. Zhang, J. Ilavsky, G.G. Long, J.P.G. Quintana, A.J. Allen, and P.R. Jemian: Glassy carbon as an absolute intensity calibration standard for small-angle scattering. *Metall. Mater. Trans. A* **41A** (5), 1151 (2010).
15. L.Y. Wang, M.M. Li, and J. Almer: In situ characterization of Grade 92 steel during tensile deformation using concurrent high energy X-ray diffraction and small angle X-ray scattering. *J. Nucl. Mater.* **440**(1–3), 81 (2013).

https://doi.org/10.1557/jmr.2015.50 Published online by Cambridge University Press

16. J.T. Busby: Advanced materials for nuclear reactor systems: Alloys by design to overcome past limitations. In *International Conference on Fast Reactors and Related Fuel Cycles (FR09): Challenges and Opportunities*, Japan, 2009.
17. National Institute of Standards and Technology: *Single Crystal Diffractometer Alignment Standard – Ruby Sphere*, USA, 2001. https://www-s.nist.gov/srmors/view_detail.cfm?srm=1990.
18. H. Sharma, R.M. Huizenga, and S.E. Offerman: A fast methodology to determine the characteristics of thousands of grains using three-dimensional X-ray diffraction. I. Overlapping diffraction peaks and parameters of the experimental setup. *J. Appl. Crystallogr.* **45**, 693 (2012).
19. H. Sharma, R.M. Huizenga, and S.E. Offerman: A fast methodology to determine the characteristics of thousands of grains using three-dimensional X-ray diffraction. II. Volume, centre-of-mass position, crystallographic orientation and strain state of grains. *J. Appl. Crystallogr.* **45**, 705 (2012).
20. J. Ilavsky and P.R. Jemian: Irena: Tool suite for modeling and analysis of small-angle scattering. *J. Appl. Crystallogr.* **42**, 347 (2009).
21. S.E. Offerman and H. Sharma: Grain nucleation and growth of individual austenite and ferrite grains studied by 3DXRD microscopy at the ESRF. In *In-situ Studies with Photons, Neutrons and Electrons Scattering*, T. Kannengiesser, S.S. Babu, Y. Komizo, and A.J. Ramirez eds.; Springer-Verlag: Berlin, 2010; p. 41.
22. U.F. Kocks, C.N. Tomé, H.-R. Wenk, and H. Mecking: *Texture and Anisotropy: Preferred Orientations in Polycrystals and Their Effect on Materials Properties* (Cambridge University Press, UK, 2000).
23. C. Mieszczynski, G. Kuri, C. Degueldre, M. Martin, J. Bertsch, C.N. Borca, D. Grolimund, C. Delafoy, and E. Simoni: Irradiation effects and micro-structural changes in large grain uranium dioxide fuel investigated by micro-beam X-ray diffraction. *J. Nucl. Mater.* **444**(1–3), 274 (2014).
24. E.D. Specht, F.J. Walker, and W.J. Liu: X-ray microdiffraction analysis of radiation-induced defects in single grains of polycrystalline Fe. *J. Synchrotron Radiat.* **17**, 250 (2010).
25. H. Peisl: Defect properties from x-ray scattering experiments. *J. Phys. Colloques.* **37**(C7), 47–53 (1976).
26. D. Grasse, B. Vonguerard, and J. Peisl: Interstitial clustering in cascades in fast-neutron irradiated aluminum by diffuse-x-ray scattering. *J. Nucl. Mater.* **108**(1–2), 169 (1982).
27. R.I. Barabash, G.E. Ice, and F.J. Walker: Quantitative microdiffraction from deformed crystals with unpaired dislocations and dislocation walls. *J. Appl. Phys.* **93**(3), 1457 (2003).
28. F. Hofmann, S. Keegan, and A.M. Korsunsky: Diffraction post-processing of 3D dislocation dynamics simulations for direct comparison with micro-beam Laue experiments. *Mater. Lett.* **89**, 66 (2012).
29. W.V. Vaidya and K. Ehrlich: Radiation-induced recrystallization, its cause and consequences in heavy-ion irradiated 20-percent cold-drawn steels of type 1.4970. *J. Nucl. Mater.* **113**(2–3), 149 (1983).
30. J. Rest: Derivation of analytical expressions for the network dislocation density, change in lattice parameter, and for the recrystallized grain size in nuclear fuels. *J. Nucl. Mater.* **349** (1–2), 150 (2006).
31. A.R. Stokes and A.J.C. Wilson: The diffraction of X rays by distorted crystal aggregates – I. *Proc. Phys. Soc.* **56**, 174 (1944).
32. L. Hsiung, S. Tumey, M. Fluss, Y. Serruys, and F. Willaime: HRTEM study of the role of nanoparticles in ODS ferritic steel. Presented at the *2010 MRS Fall Meeting, USA*, 2010.
33. X. Pan, X. Wu, K. Mo, X. Chen, J. Almer, J. Ilavsky, D.R. Haeffner, and J.F. Stubbins: Lattice strain and damage evolution of 9-12%Cr ferritic/martensitic steel during in situ tensile test by X-ray diffraction and small angle scattering. *J. Nucl. Mater.* **407**(1), 10 (2010).
34. L. Wang, M. Li, and J. Almer: Investigation of deformation and microstructural evolution in Grade 91 ferritic-martensitic steel by in situ high-energy X-rays. *Acta Mater.* **62**, 239 (2014).
35. S.L. Wong and P.R. Dawson: Influence of directional strength-to-stiffness on the elastic–plastic transition of fcc polycrystals under uniaxial tensile loading. *Acta Mater.* **58**(5), 1658–1678 (2010), ISSN 1359-6454. http://dx.doi.org/10.1016/j.actamat.2009.11.009.
36. U.F. Kocks: The relation between polycrystal deformation and single-crystal deformation. *Metall. Mater. Trans. B* **1**(5), 1121–1143 (1970).
37. U.F. Kocks, G.R. Canova, and J.J. Jonas: Yield vectors in F.C.C. crystals. *Acta Metall.* **31**(8), 1243–1252 (1983).
38. H. Ritz, P. Dawson, and T. Marin: Analyzing the orientation dependence of stresses in polycrystals using vertices of the single crystal yield surface and crystallographic fibers of orientation space. *J. Mech. Phys. Solids* **58**(1), 54–72 (2010), ISSN 0022-5096. http://dx.doi.org/10.1016/j.jmps.2009.08.007.
39. R.E. Stoller, F.J. Walker, E.D. Specht, D.M. Nicholson, R.I. Barabash, P. Zschack, and G.E. Ice: Diffuse X-ray scattering measurements of point defects and clusters in iron. *J. Nucl. Mater.* **367**, 269 (2007).
40. M.A. Krivoglaz: *X-ray and Neutron Diffraction in Nonideal Crystals* (Springer Verlag, Germany, 1996).
41. J. Spino and D. Papaioannou: Lattice parameter changes associated with the rim-structure formation in high burn-up UO_2 fuels by micro X-ray diffraction. *J. Nucl. Mater.* **281**(2–3), 146 (2000).
42. M. Song, Y.D. Wu, D. Chen, X.M. Wang, C. Sun, K.Y. Yu, Y. Chen, L. Shao, Y. Yang, K.T. Hartwig, and X. Zhang: Response of equal channel angular extrusion processed ultrafine-grained T91 steel subjected to high temperature heavy ion irradiation. *Acta Mater.* **74**, 285 (2014).
43. K.G. Field, L.M. Barnard, C.M. Parish, J.T. Busby, D. Morgan, and T.R. Allen: Dependence on grain boundary structure of radiation induced segregation in a 9 wt.% Cr model ferritic/martensitic steel. *J. Nucl. Mater.* **435**(1–3), 172 (2013).
44. A. Alsabbagh, R.Z. Valiev, and K.L. Murty: Influence of grain size on radiation effects in a low carbon steel. *J. Nucl. Mater.* **443** (1–3), 302 (2013).
45. W. Han, M.J. Demkowicz, N.A. Mara, E. Fu, S. Sinha, A.D. Rollett, Y. Wang, J.S. Carpenter, I.J. Beyerlein, and A. Misra: Design of radiation tolerant materials via interface engineering. *Adv. Mater.* **25**(48), 6975 (2013).
46. G.K. Williamson and W.H. Hall: X-ray line broadening from filed aluminium and wolfram. *Acta Metall.* **1**(1), 22–31 (1953), ISSN 0001-6160. http://dx.doi.org/10.1016/0001-6160(53http://dx.doi.org/10.1016/0001-6160(53)90006-6.
47. B.E. Warren and B.L. Averbach: The effect of cold-work distortion on X-ray patterns. *J. Appl. Phys.* **21**, 595–599 (1950). DOI:http://dx.doi.org/10.1063/1.1699713.
48. T. Ungár and A. Borbély: The effect of dislocation contrast on x-ray line broadening: A new approach to line profile analysis. *Appl. Phys. Lett.* **69**, 3173 (1996). (doi: 10.1063/1.117951).
49. S.L. Wong, J-S. Park, M.P. Miller, and P.R. Dawson: A framework for generating synthetic diffraction images from deforming polycrystals using crystal-based finite element formulations. *Comput. Mater. Sci.* **77**, 456–466 (2013), ISSN 0927-0256. http://dx.doi.org/10.1016/j.commatsci.2013.03.019.
50. M. Obstalecki, S.L. Wong, P.R. Dawson, and M.P. Miller: Quantitative analysis of crystal scale deformation heterogeneity during cyclic plasticity using high-energy X-ray diffraction and finite-element simulation. *Acta Mater.* **75**, 259–272 (2014), ISSN 1359-6454. http://dx.doi.org/10.1016/j.actamat.2014.04.059.

https://doi.org/10.1557/jmr.2015.50 Published online by Cambridge University Press

51. N.R. Barton, A. Arsenlis, and J. Marian: A polycrystal plasticity model of strain localization in irradiated iron. *J. Mech. Phys. Solids* **61**(2), 341–351 (2013), ISSN 0022-5096, http://dx.doi.org/10.1016/j.jmps.2012.10.009.
52. R.A. Lebensohn and C.N. Tomé: A self-consistent anisotropic approach for the simulation of plastic deformation and texture development of polycrystals: Application to zirconium alloys. *Acta Metall. Mater.* **41**(9), 2611–2624 (1993), ISSN 0956-7151. http://dx.doi.org/10.1016/0956-7151(93http://dx.doi.org/10.1016/0956-7151(93)90130-K.
53. P. Dawson, M. Miller, T-S. Han, and J. Bernier: An accelerated methodology for the evaluation of critical properties in polyphase alloys. *Metall. Mater. Trans. A* **36**(7), 1627–1641 (2005).
54. C. Efstathiou, D.E. Boyce, J-S. Park, U. Lienert, P.R. Dawson, and M.P. Miller: A method for measuring single-crystal elastic moduli using high-energy X-ray diffraction and a crystal-based finite element model. *Acta Mater.* **58**(17), 5806–5819 (2010), ISSN 1359-6454. http://dx.doi.org/10.1016/j.actamat.2010.06.056.

https://doi.org/10.1557/jmr.2015.50 Published online by Cambridge University Press